ARTICLE

OPEN

Check for updates

Highly charged 180 degree head-to-head domain walls in lead titanate

Kalani Moore[1✉], Michele Conroy [1], Eoghan N. O'Connell [1], Charlotte Cochard[2], Jennifer Mackel[2], Alan Harvey[1], Thomas E. Hooper [3], Andrew J. Bell [3], J. Marty Gregg [2] & Ursel Bangert [1✉]

Charged domain walls (DWs) in ferroelectric materials are an area of intense research. Microscale strain has been identified as a method of inducing arrays of twin walls to meet at right angles, forming needlepoint domains which exhibit novel material properties. Atomic scale characterisation of the features exhibiting these exciting behaviours was inaccessible with the piezoresponse force microscopy resolution of previous work. Here we use aberration corrected scanning transmission electron microscopy to observe short, stepped, highly charged DWs at the tip of the needle points in ferroelectric $PbTiO_3$. Reverse Ti^{4+} shift polarisation mapping confirms the head-to-head polarisation in adjacent domains. Strain mapping reveals large deviations from the bulk and a wider DW with a high Pb^{2+} vacancy concentration. The extra screening charge is found to stabilise the DW perpendicular to the opposing polarisation vectors and thus constitutes the most highly charged DW possible in $PbTiO_3$. This feature at the needle point junction is a 5 nm × 2 nm channel running through the sample and is likely to have useful conducting properties. We envisage that similar junctions can be formed in other ferroelastic materials and yield exciting phenomena for future research.

[1] Department of Physics, Bernal Institute, School of Natural Sciences, University of Limerick, Limerick, Ireland. [2] Centre for Nanostructured Media, Queens University Belfast, Belfast, UK. [3] School of Chemical and Process Engineering, University of Leeds, Leeds, UK. ✉email: kalanimoore@gmail.com; Ursel.Bangert@ul.ie

'The interface is the device' said Herbert Kroemer in his Nobel laureate speech in 2000[1]. He was then referring to semiconductor heterostructures, however, this idea has held true for ferroic materials where domain walls (DWs) have been found to possess a high degree of functional tunability with extremely low dielectric loss[2–7]. Complex domain junctions have been seen to induce exotic behaviour in ferroelectrics, from novel dipolar topologies (vortex–antivortex chains) to metallic behaviour near needle-point domains in VO_2 and conducting vortex cores[8–13]. Hindering applications[11,14,15] of these novel properties is the lack of knowledge of atomic-level composition. Identifying the localised symmetry breaking of ions is key to unlocking the drastic changes of conductivity, magnetism and strain observed in DWs[3,16,17].

In $PbTiO_3$ (PTO) single crystals, needle-tip domains form due to arrays of 90° ferroelastic twin domains meeting at right angles. These regions have been highlighted by Salje et al.[18,19] as potentially exciting, as they could constitute DW-based Josephson junctions in systems where some of the DW components are in the superconducting state. Recent works have focused on needle points enclosed inside another domain[20]. In contrast, the super-conducting charged needle points (CNPs) form between arrays of twin walls; two DWs bend towards each other to intersect a third, perpendicular twin DW, which results in CNP junctions. The novel properties present at CNP junctions arise from the polarisation discontinuity present, even in purely ferroelastic materials, where flexoelectric polarisation between nanoscale twin walls is significant[21–23].

Charged DWs have an energy density of one order in magnitude higher than neutral DWs, meaning they do not arise spontaneously in proper ferroelectrics[6,24,25]. In this paper, we exploit microscale elastic strain to stabilise nanoscale charged DWs. We then investigate the DW structure of the CNPs themselves, using atomic resolution polarisation mapping via aberration-corrected scanning transmission electron microscopy (STEM)[26]. Shifts in the Ti^{4+} atomic columns show that the charged DW is polarised head-to-head with a high density of ionic vacancies trapped between the directly opposing electric fields.

Results
Figure 1a shows an array of CNPs that formed in the TEM lamella cut from a single crystal of PTO. See 'Methods' section for details on crystal growth and sample preparation. PTO domains have a large spontaneous polarisation of $0.75\,cm^{-2}$[27–29]. Four possible in-plane polarisations are allowed, which align with the major zones axes. DWs are identified by their bright intensity in the MAADF STEM image. The structural mismatch between domains causes strain at the DWs which de-channels the probe, causing additional scattering[30,31]. Hence, brightness in Fig. 1a, b corresponds to increased strain. The array of stepped CNPs exhibit bright intensity at their tips. In Fig. 1b, c the reason for this becomes clear. The 180° DW is orientated along the [001] direction, 45° different to the twin DWs. This orientation causes a ~5-nm step in the twin DW boundary with an enormous resultant strain of ~29%. The stepped DW represents a 5 nm × 2 nm channel running through the sample. Figure 1c is a quantitative map of the strain measured from the atomic positions with respect to the cubic unit cell spacing. Six percent of the measured strain difference can be attributed to the rotation of the longer tetragonal c parameter in different domains. The nature of the CNP as a 180° DW is confirmed by the 6% horizontal spontaneous strain measured in both the A2 and A3 domains, perpendicular to the DW. The polarisation must be opposite in A2 and A3 to keep the longer A1/A3 DW neutral.

In Fig. 2, the structural effects of stresses induced by a and c unit cell parameters meeting across multiple DWs at the needle tip are demonstrated. Figure 2b is a Fourier filtered image[32] showing the evolution of the (100) planes at the CNP. It clearly demonstrates the rupture and recovery of the structure without dislocations. Figure 2a, c, d compare the variation in strain, structural rotation and tetragonality, respectively, between the 180° charged DW and the neutral twin DW. They are measured from the atomic column coordinates determined by 2D Gaussian fitting for sub-pixel accuracy[33]. Uncertainty is ~1.3% for the strain and 0.026 for the c/a ratio, explaining some of the in-domain fluctuations. The red profile covers the needle domain (A2) from 0 to 9 nm and the larger A3 domain from 10 to 20 nm. The charged DW lies approximately between 9 and 10 nm. The neutral DW in the dotted blue profile occurs from 8 to 9 nm.

The exact polarisation vectors are determined by reverse Ti-shift mapping in Fig. 3[34,35]. Figure 3a displays the relative positions of Fig. 3b, c, from which the polarisation of the CNP is verified as H–H. The depolarising electric field traps negative carriers at the H–H DW. Figure 3d, e provides a visual explanation for how the Ti shift forms a dipole in the MAADF image. The complete polarisation map is available in Supplementary Fig. 1.
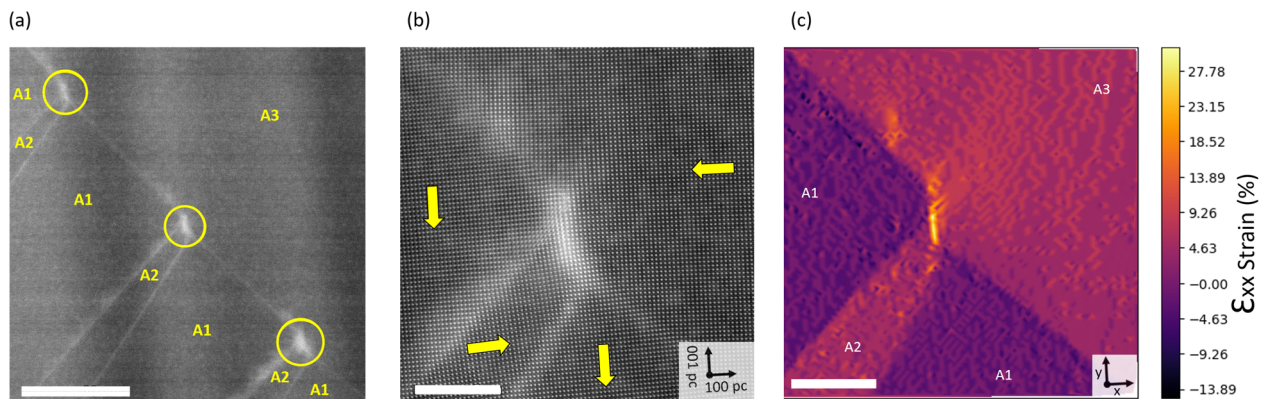

Fig. 1 Medium and high-resolution images of the array of charged needle points. a Medium angle annular dark field (MAADF) scanning transmission electron microscopy (STEM) image of an array of charged needle-point domains. Scale bar = 40 nm. **b** High-resolution MAADF STEM image showing atomic-level detail of the structural changes across the 180° charged domain wall. This domain wall forms a "nanochannel" of cross-section 5 nm × 2 nm running through the sample. Spontaneous polarisation interpreted from (**c**) marked with yellow arrows. Scale bar = 8 nm. **c** Quantitative strain map of (**b**), measured with respect to the theoretical cubic lattice parameter at room temperature (3.929 Å). There is ~29% strain at the junction where the structure ruptures. Scale bar = 8 nm.
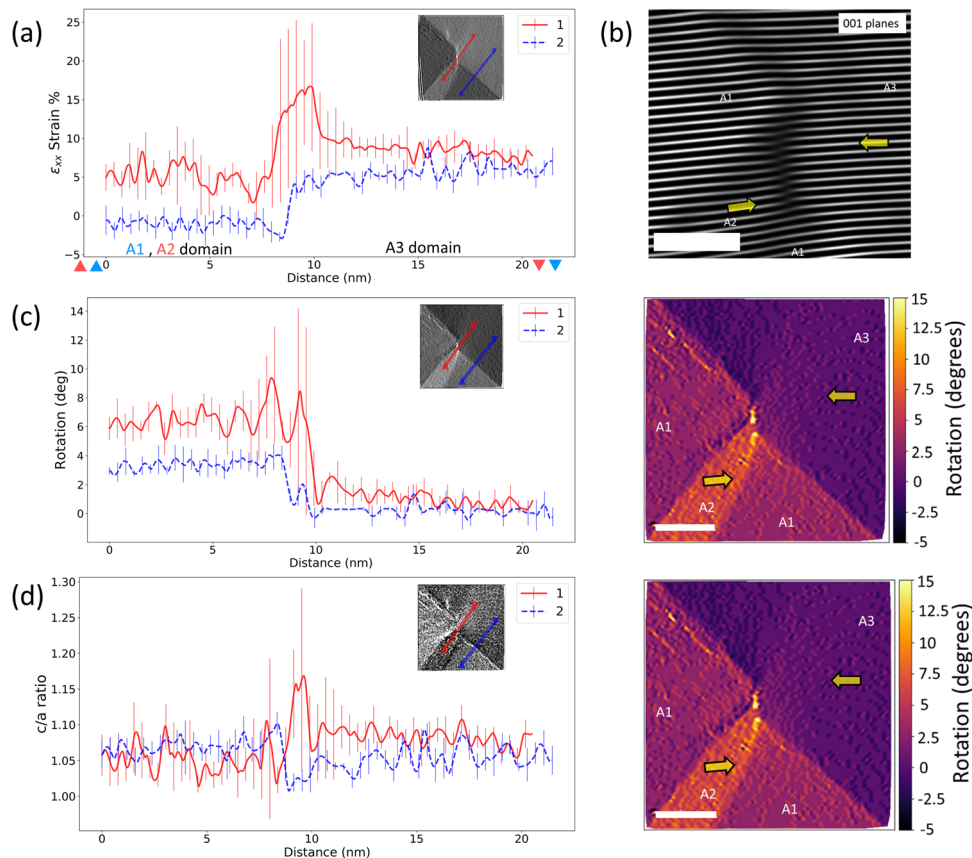
Fig. 2 Structural differences between the charged needle point and a neutral twin domain wall boundary. Comparison of structural parameters across the charged needle point (red, solid line) and the neutral twin boundary (blue, dotted line). Inset are maps of the parameter indicating where the profiles displayed in the graphs are extracted from. **a** ε_{xx} strain profiles. **b** Fourier filtered image showing the (001) planes at the charged needle point. Scale bar = 4 nm. Despite the massive strain there is no dislocation present. **c** Profiles and map of the relative structural rotation. Scale bar = 8 nm. **d** Profiles and map of the tetragonality of each unit cell measured by c/a ratio. Scale bar = 8 nm. Error bars are $+/-$ the standard deviation of the 100 pixel values (~4 unit cells) over which the profile is averaged. They are placed at approximately each unit cell along the profile.

Figure 4 shows intensity differences of the Pb atomic columns across the CNP. In Fig. 4a, the contributions from de-channelling have been removed from Fig. 1b (see Supplementary Fig. 2 and Supplementary note 1 for details). Figure 4b maps out the integrated and normalised column intensities which are proportional to the number of Pb atoms present. The intensity drop of 10% is compared to Bi vacancy simulations by Rojac et al.[30] and corresponds to the presence of ~20 +/− 5% Pb vacancies ($V_{Pb}{}^{2-}$) per atomic column. Vacancies also seem to be present at the A2/A1 DWs, which become charged as they bend to form a needle point. Figure 4c compares intensity profiles across the Pb columns of (1) the charged A2/A3 DW and A1 domain, and (2) the neutral A1/A3 DW. The profile positions are indicated in Fig. 4a.

The STEM probe can be used to switch domains and move DWs in situ. This switching process is shown in Fig. 5, which shows the DW configuration in the same area (a) "before" and (b) "after" switching. During the process, the A3/A4 180° DW (dotted yellow line) moves from the top left to the bottom right of the frame. In doing so it causes the needle-point A2 domain to change from a neutral H–T state into a H–H CNP.

Discussion

The extent of the H–H character at the CNP is remarkable. The vertical A2/A3 DW in Fig. 3a is almost perpendicular to the 180° polarisation vectors in the adjacent domains. The charged state appears to constrain the charged wall to the vertical $(100)_{pc}$ plane, hence creating the observed step. For the H–H DW to be

stabilised the polarisation on either side must be fully screened, meaning it should contain $2 \times P_s$ of negative charge[36]. The charge at the PTO DW is then $\sigma_s = (2)(0.75\ cm^{-2})(0.39\ nm)^2 = 2.28 \times 10^{-19}\ C$ per unit cell. Structural analysis in Fig. 2 and the de-channelling intensity in Fig. 1b suggest that the domain wall is 2 nm/5 unit cells in width but Fig. 4b suggests that vacancies are confined to 2 or 3 unit cells at the DW. Even assuming the charge is spread over 4 unit cells, the charge density $\rho = \frac{2.28 \times 10^{-19}}{4(1.6 \times 10^{-19})} = 0.36e^-$ per unit cell. where $e^- = 1.6 \times 10^{-19}\ C$, elementary charge. Eighteen-percent Pb vacancies ($V_{Pb}{}^{2-}$) would provide this charge. Examining Fig. 4b, c shows that the Pb intensity drops by ~10% at the H–H DW. Pb columns are comparable to Bi in $BiFeO_3$, where a 10% intensity drop corresponds to 20 +/− 5% vacancies[30]. Therefore, the experimental evidence supports the presence of Pb vacancies stabilising the H–H DW at the CNP.

The properties observed are very different to those at the H–H DW identified in lead zirconate titanate by Jia et al.[37]. We note that Sifuna et al. recently calculated that a 2D electron gas would be found screening PTO H–H DWs but did not take into account the 5% vacancies present intrinsically in single-crystal PTO due to Pb and O volatility[38,39]. Vacancies provide a readily available source for charge screening and are energetically cheaper than creating free electrons[40]. Indeed, in Fig. 4b, we see a variation in intensities within domains. Vacancies are clearly concentrated at the bent (and therefore charged) A1/A2 DWs that make up the needle. They are also found in the strained area in the upper left A1 domain. By contrast, the less strained, neutral A1/A3 DW
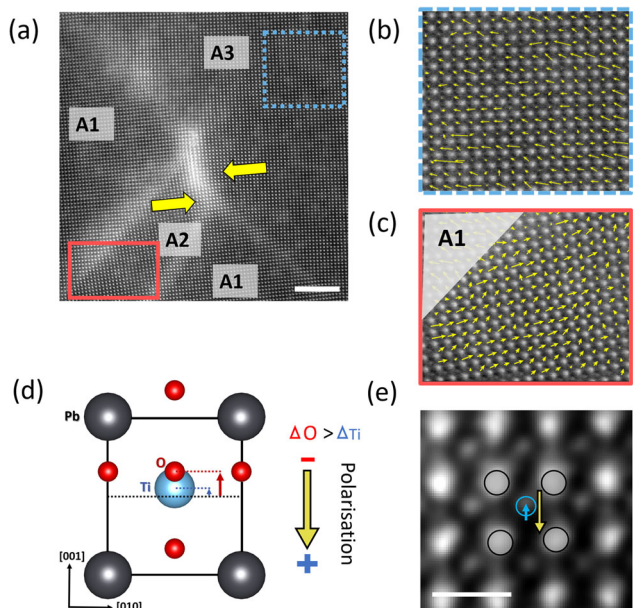
Fig. 3 Polarisation map of domains either side of the charged needle point. a Medium angle annular dark field image of the needle-point domain structure. Boxes indicate the areas of least strain considered in polarisation mapping, and yellow arrows denote the polarisation (P_s) directions. Scale bar = 5 nm. **b, c** Unit cell polarisation maps of the highlighted areas in domains A3 (blue, dashed outline) and A2 (red, solid outline), respectively. **d, e** Schematics showing the unit cell deformation in tetragonal PbTiO$_3$ and the resulting polarisation in the direction opposite to the Ti shift. ΔO and ΔTi refer to the displacements of the oxygen and titanium columns from their neutral positions, respectively. Scale bar = 0.5 nm.

shows no localisation of vacancies at the wall. These observations point towards a combined contribution of strain and electrostatic energy in holding vacancies at DWs around the CNP, in agreement with theoretical calculations[41]. Thus there are likely O and Ti vacancies present too.

The enormous screening charge density has stabilised the array of CNPs and allowed otherwise elastically impossible properties to stabilise in the constituent DWs. Figure 2a–c offers an insight into the structural deformation by comparing profiles of the spontaneous strain, tetragonality and structural rotation across the CNP (red) and a normal, neutral twin wall (dotted, blue). The spontaneous strain ε_{xx} in Fig. 2a is measured with respect to the theoretical cubic room temperature unit cell spacing (3.929 Å). The average c and a parameters are 5% and −1%, respectively, in the areas furthest from the disruptive influence of the CNP, in agreement with theory (see Supplementary Fig. 3). Profile 2 in Fig. 2a exhibits the expected sharp transition from a to c spacing across the twin wall. Approaching the CNP, profile 1 in Fig. 2a drops below 2.5% at 7 nm before increasing drastically to 17% at the DW itself around 9.5 nm. There is a prolonged strain gradient away from the DW and even at 20 nm (10 nm away from the CNP) the structure has not fully relaxed back to 5%. In Fig. 1c we observe that in the A3 domain, in front of the CNP, strain extends mostly in the x direction. There is a larger strain gradient in the y direction, as the structure is relaxed directly above the CNP in the A3 domain.

Whilst there is only a very small difference in strain in the H–H domains (A2 and A3), Fig. 2c reveals that there is a severe rotation difference of 6° between them. The measured rotation is as high as 9° at the tip of the needle where there is an extra distortion from the ruptured structure. This can be seen clearly by inspecting the darker areas of the [001]$_{pc}$ lattice planes in Fig. 2b.
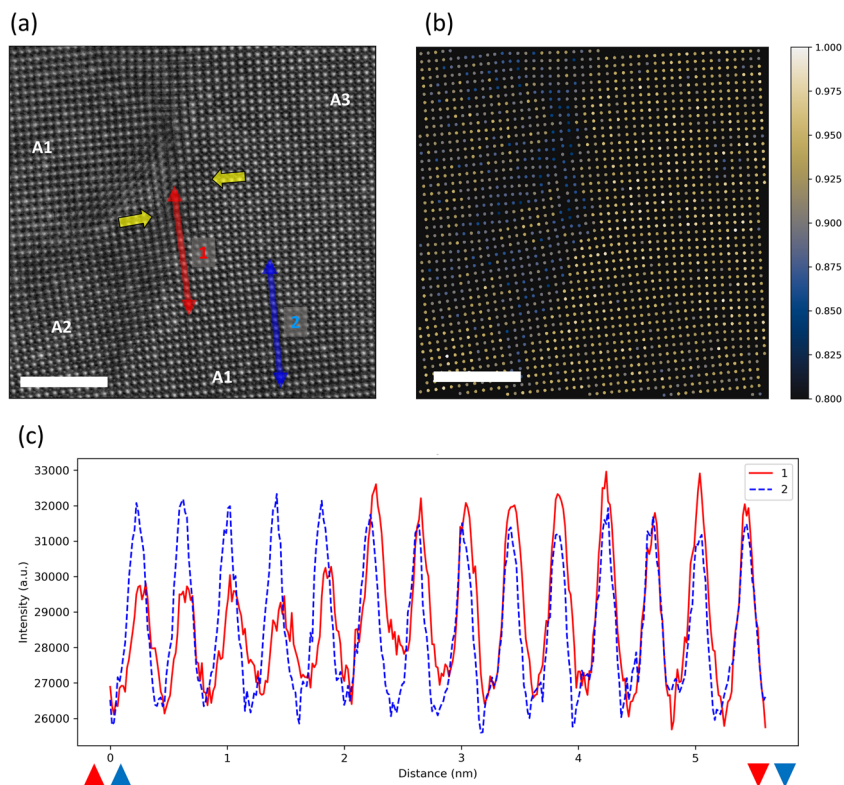

Fig. 4 Evidence for vacancies at the charged needle point. a Background subtracted medium angle annular dark field image of a charged needle point with overlay showing the location of the line profiles in (**c**). **b** Integrated intensity of each Pb atomic column, normalised to the maximum. **c** Line profiles across a charged domain wall (1, red) and across a neutral A1/A3 DW (2, blue). Scale bars = 8 nm.
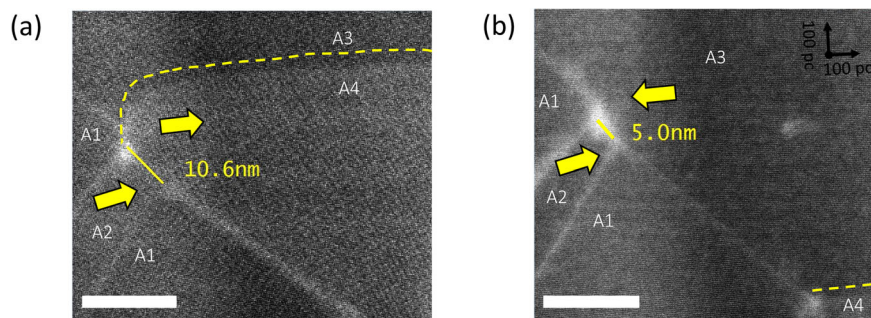
Fig. 5 In situ switching narrows the charged needle point. The domain wall region (**a**) before and (**b**) after switching by the electron beam. Distance labels indicate the length of the needle tip in each case. From the initial neutral configuration in (**a**), the junction becomes charged in (**b**) after movement of the 180° (dashed yellow) domain wall to the bottom right corner. The needle point narrows from 10.6 nm to 5 nm in response. Scale bars = 20 nm.

The strain gradient extending into the A3 domain is mirrored by a 2° rotation gradient in profile 1 starting from 11 nm.

Figure 2d compares the c/a ratio of each unit cell, nominally a uniform 1.06, around the junction. Looking first at the map, this is clearly not the case. Overall, the needle domain has been compressed into a more cubic shape, while the adjacent domains have been pulled into a more tetragonal shape. Directly in front of the CNP the strain gradient into A3 means that the unit cells are highly tetragonal there, $c/a \approx 1.08$, but less tetragonal than normal at shallow angles from the CNP, close to the twin boundary, $c/a \approx 1.05$. The black lines tracing the twin DWs show their almost cubic structure. From 7 to 11 nm in profile 1, Fig. 2c, there are sharp changes in c/a, ranging from almost cubic to extremely tetragonal, $c/a \approx 1.10$ and 1.16. The variance comes from the interplay of x and y strains across the charged DW; there is a broad peak of large x-strain whereas the y-strain (Supplementary Fig. 4) is localised at 8 nm in profile 1, Fig. 2c. Again, we observe a gradient away from the CNP where profile 1 and 2 in Fig. 2c tend towards each other from 10 to 20 nm. Overall, the charged DW has a width of ~2 nm and is clearly wider than the neutral DW.

Strain at the ruptured lattice in Fig. 1c is 29%. Taking Young's modulus (E) as 80 GPa, the stress $= E * 0.29 \approx 23$ GPa. Comparatively, the 10% strain in the adjacent unit cell means the stress ≈ 8 GPa, where the structure remains intact. These results agree with previous observations that exceeding the theoretical shear strength of PTO of ~14 GPa causes the ruptured structure[29]. Surprisingly, inspection of Fig. 2b reveals that no dislocation is present and the structure recovers from the disruptive CNP stresses when it meets the neutral twin DW along the diagonal $(110)_{pc}$ plane. Large strain gradients may also lead to a flexoelectric contribution to the polarisation.

The in situ switching observed in Fig. 5 sheds new light on the formation dynamics of the CNPs and provides evidence for the energetics governing their size. In Fig. 5a, the initial DW configuration features a mostly neutral 180° DW (yellow dotted line) between domains A3 and A4. This DW is strongly bent to join to the kinked junction and this bending makes the A3/A4 partially tail-to-tail in character. The dynamic free charge gradients induced by the STEM beam can act as a switching mechanism in ferroelectrics. After multiple STEM scans, most of the area in the original A4 domain in Fig. 5a switched 180° and the 180° neutral DW moved down the bottom part of the image. This movement causes the A2 domain to become directly H–H with the A3 domain and so it moves to reduce the area of the charged DW, narrowing the needle point from 10.6 to 5 nm. The narrowing of the tip bends the 90° H–T, A1/A2 DWs even further from their neutral straight orientation. The narrowed needle point is therefore a balance between the electrostatic cost of bending the

H–T walls and the energy gained by reducing the area of the charged tip. It appears likely that the intrinsically large vacancy concentration in PTO allows Pb atoms to move away and vacancies to quickly migrate toward the CNP to provide the screening charge necessary to stabilise the new orientation. To the authors' knowledge, this type of dynamic switching of DW configurations under the STEM beam in a lamella to balance stress and electrostatics in moving DWs has never been reported.

A larger field-of-view is presented in Fig. 6a, beside a simplified model in Fig. 6b, which attempts to clarify the domain arrangement that leads to CNP formation. These CNPs (red) can be thought of as nanochannels running through the lamella. The wider context behind the creation of this array is that in the thin lamella the domains are constrained to only form in-plane polarisations[42]. When thin ferroelectric samples are subject to lateral mechanical strain they form arrays of H–T a_1–a_2 twins[43]. When the sample does not have edges that are parallel with the major crystal axes, the arrays of twins attempt to form in two directions. Where these right-angled arrays of twin walls intersect, no geometry will allow the twins to join without assembling the array of CNP domains. Thus, a roadmap for reliably producing CNPs with nanochannels and exotic physical properties would be the growth of microscale areas of thin films. These can then be free-released from their substrates and cut into a square pattern with edges parallel to the $[110]_{pc}$ and $[-110]_{pc}$ directions. A useful parameter with this method is the ability to precisely control the film thickness and hence the CNP period. In this work, cracks along the $[110]_{pc}$ and $[-110]_{pc}$ directions provided the required shape (Supplementary Fig. 5) while similar approaches produced CNPs in various materials[9,13,44–47]. The large charge density combined with the enhanced conductivity of ionic carriers at strained DWs point towards potentially exciting conducting characteristics to be further investigated in CNPs[18].

Methods

Crystal growth. PTO single crystals were grown using the self-flux method. One hundred and fifty grams of powder with a 4:1 (PbO:TiO$_2$) molar ratio was placed inside a 50 cm^3 platinum crucible and subsequently buried in a titania powder bed inside a sealed alumina crucible. The crucibles were placed inside a box furnace and heated to 1080 °C at a rate of 180 °C/h and dwelled for 12 h. The furnace was then step-cooled to 1040 °C and immediately slow-cooled from 1040 to 920 °C over 141 h (0.85 °C/h) and finally cooled to room temperature over 72 h (12.5 °C/h). PbTiO$_3$ crystals were extracted gradually from the solidified flux by sonicating in warm acetic acid and filtering.

Electron microscopy. The bulk single-crystal PTO was initially imaged using a Thermo Fisher Scientific (TFS) Helios G4 CX at 5 kV in secondary electron mode. An electron transparent TEM lamella was prepared within the same instrument using the Ga ion source. STEM imaging was conducted using a double corrected and monochromated TFS Titan Themis cubed. The convergence angle was 24 mrad and the collection angle was 52–200 mrad using the HAADF detector. The
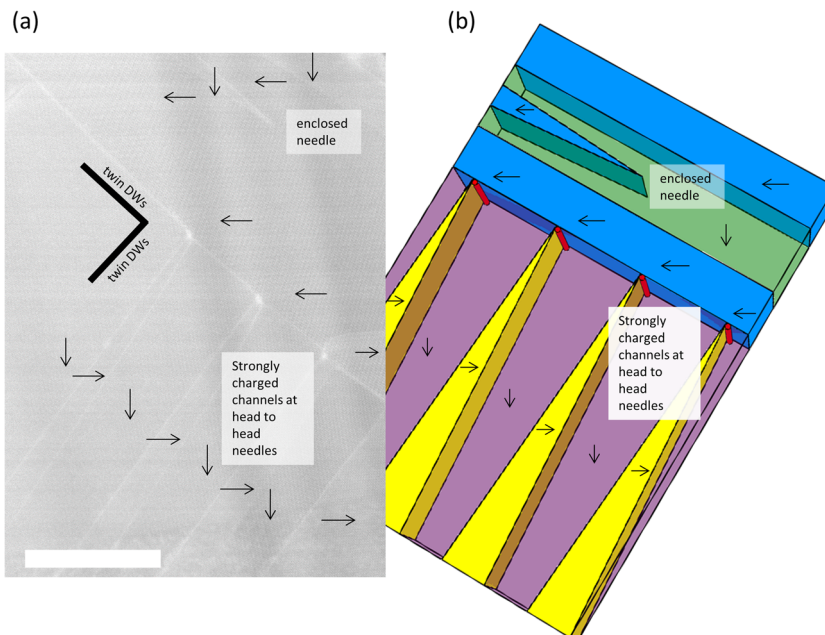
Fig. 6 Overview of the domain structure that causes charged needle points. a Lower magnification scanning transmission electron microscopy image showing the wider domain structure with both an enclosed needle (top) and an array of charged needle points. **b** 3D model of the domain configuration in (**a**) leading to charged nanochannels at the charged needle points. The model is tilted with respect to the real viewing direction to show the 3D structure. Scale bar = 100 nm.

screen current was ~ 41 pA. Atom position finding and 2D Gaussian refinement were completed with the Atomap Python package[33]. Image analysis and mapping, as well as polarisation vector analysis, were completed using the TEMUL Toolkit Python package[48]. A walkthrough of the processing steps will be available at the TEMUL Toolkit repository (www.github.com/PinkShnack/TEMUL). Strain analysis for Supplementary Fig. 1 was carried out by geometric phase analysis using the Stem Cell program[49].

Data availability

The charged needle point STEM dataset and analysis can be found at https://temul-toolkit.readthedocs.io/en/latest/PTO_Junction_moore.html. Other datasets supporting the findings of this study are available from the corresponding authors upon reasonable request.

References

1. Kroemer, H. Nobel Lecture: Quasielectric fields and band offsets: teaching electrons new tricks. *Rev. Mod. Phys.* **73**, 783 (2001).
2. Meier, D. Functional domain walls in multiferroics. *J. Phys. Condens. Matter* **27**, 463003 (2015).
3. Li, L. et al. Giant resistive switching via control of ferroelectric charged domain walls. *Adv. Mater.* **28**, 6574–6580 (2016).
4. Sharma, P. et al. Nonvolatile ferroelectric domain wall memory. *Sci. Adv.* **3**, e1700512 (2017).
5. Tselev, A. et al. Microwave a.c. conductivity of domain walls in ferroelectric thin films. *Nat. Commun.* **7**, 11630 (2016).
6. Catalan, G., Seidel, J., Ramesh, R. & Scott, J. F. Domain wall nanoelectronics. *Rev. Mod. Phys.* **84**, 119–156 (2012).
7. Gu, Z. et al. Resonant domain-wall-enhanced tunable microwave ferroelectrics. *Nature* **560**, 622–627 (2018).
8. Chang, L.-W., Nagarajan, V., Scott, J. F. & Gregg, J. M. Self-similar nested flux closure structures in a tetragonal ferroelectric. *Nano Lett.* **13**, 2553–2557 (2013).
9. McGilly, L. J., Schilling, A. & Gregg, J. M. Domain bundle boundaries in single crystal BaTiO$_3$ lamellae: searching for naturally forming dipole flux-closure/quadrupole chains. *Nano Lett.* **10**, 4200–4205 (2010).
10. Wei, X.-K. et al. Néel-like domain walls in ferroelectric Pb(Zr,Ti)O$_3$ single crystals. *Nat. Commun.* **7**, 12385 (2016).
11. Balke, N. et al. Enhanced electric conductivity at ferroelectric vortex cores in BiFeO$_3$. *Nat. Phys.* **8**, 81–88 (2012).
12. Stolichnov, I. et al. Bent ferroelectric domain walls as reconfigurable metallic-like channels. *Nano Lett.* **15**, 8049–8055 (2015).
13. Tselev, A. et al. Mesoscopic metal–insulator transition at ferroelastic domain walls in VO$_2$. *Acs Nano* **40**, 25 (2019).
14. Li, Y. et al. Rewritable ferroelectric vortex pairs in BiFeO$_3$. *npj Quantum Mater.* **2**, 43 (2017).
15. Chen, W. J., Zheng, Y. & Wang, B. Vortex domain structure in ferroelectric nanoplatelets and control of its transformation by mechanical load. *Sci. Rep.* **2**, 796 (2012).
16. Jiang, J. et al. Temporary formation of highly conducting domain walls for non-destructive read-out of ferroelectric domain-wall resistance switching memories. *Nat. Mater.* **17**, 49–55 (2018).
17. Zhang, Y. et al. Intrinsic Conductance of Domain Walls in BiFeO$_3$. *Adv. Mater.* **31**, 1902099 (2019).
18. Salje, E. K. H. & Lu, G. in *Domain Walls: From Fundamental Properties to Nanotechnology Concepts* (2020).
19. Aird, A. & Salje, E. K. H. Sheet superconductivity in twin walls: experimental evidence of WO$_{3-x}$. *J. Phys.: Condens. Matter* **10**, L377 (1998).
20. Gao, P. et al. Ferroelastic domain switching dynamics under electrical and mechanical excitations. *Nat. Commun.* **5**, 3801 (2014).
21. Yun, S. et al. Ferroelastic twin structures in epitaxial WO$_3$ thin films. *Appl. Phys. Lett.* **107**, 252904 (2015).
22. Chu, K. et al. Enhancement of the anisotropic photocurrent in ferroelectric oxides by strain gradients. *Nat. Nanotechnol.* **10**, 972–979 (2015).
23. Bauer, A. & Pfleiderer, C. Topological structures in ferroic materials. *Topological Struct. Ferroic Mater. Springe. Ser. Mater. Sci.* **228**, 1–28 (2016).
24. Gureev, M. Y., Tagantsev, A. K. & Setter, N. Structure and energy of charged domain walls in ferroelectrics. in *2009 18th IEEE International Symposium on the Applications of Ferroelectrics* 1–6. https://doi.org/10.1109/ISAF.2009.5307622 (IEEE, 2009).
25. Kittel, C. Theory of the structure of ferromagnetic domains in films and small particles. *Phys. Rev.* **70**, 965–971 (1946).
26. Nelson, C. T. et al. Spontaneous vortex nanodomain arrays at ferroelectric heterointerfaces. *Nano Lett.* **11**, 828–834 (2011).
27. Fesenko, E. G., Gavrilyatchenko, V. G., Martinenko, M. A., Semenchov, A. F. & Lapin, I. P. Domain structure peculiarities of lead-titanate crystals. *Ferroelectrics* **6**, 61–65 (1973).
28. Hlinka, J. Domain walls of BaTiO$_3$ and PbTiO$_3$ within Ginzburg-Landau-Devonshire model. *Ferroelectrics* **375**, 132–137 (2008).
29. Tang, Y. L. et al. Observation of a periodic array of flux-closure quadrants in strained ferroelectric PbTiO$_3$ films. *Science* **348**, 547–551 (2015).
30. Rojac, T. et al. Domain-wall conduction in ferroelectric BiFeO$_3$ controlled by accumulation of charged defects. *Nat. Mater.* **16**, 322–327 (2017).
31. Williams, D. B. & Carter, C. B. *Transmission Electron Microscopy* (2009).

32. Moore, K., Conroy, M. & Bangert, U. Rapid polarization mapping in ferroelectrics using Fourier masking. *J. Microsc.* **279**, 222–228 (2020).

33. Nord, M., Vullum, P. E., MacLaren, I., Tybell, T. & Holmestad, R. Atomap: a new software tool for the automated analysis of atomic resolution images using two-dimensional Gaussian fitting. *Adv. Struct. Chem. Imaging* **3**, 9 (2017).

34. Shirane, G., Axe, J. D., Harada, J. & Remeika, J. P. Soft ferroelectric modes in lead titanate. *Phys. Rev. B* **2**, 155–159 (1970).

35. Yadav, A. K. et al. Observation of polar vortices in oxide superlattices. *Nature* **530**, 198–201 (2016).

36. Bednyakov, P. S., Sturman, B. I., Sluka, T., Tagantsev, A. K. & Yudin, P. V. Physics and applications of charged domain walls. *npj Comput. Mater.* **4**, 65 (2018).

37. Jia, C.-L. et al. Atomic-scale study of electric dipoles near charged and uncharged domain walls in ferroelectric films. *Nat. Mater.* **7**, 57–61 (2008).

38. Sifuna, J., García-Fernández, P., Manyali, G. S., Amolo, G. & Junquera, J. First-principles study of two-dimensional electron and hole gases at the head-to-head and tail-to-tail 180° domain walls in $PbTiO_3$ ferroelectric thin films. *Phys. Rev. B* **101**, 174114 (2020).

39. Holman, R. L. & Fulrath, R. M. Intrinsic nonstoichiometry in single-phase Pb $(Zr_{0.5}Ti_{0.5})O_3$. *J. Am. Ceram. Soc.* **55**, 192–194 (1972).

40. Sturman, B. & Podivilov, E. Ion and fixed electron-ion screening of charged domain walls in ferroelectrics. *mEPL (Europhysics Lett.)* **122**, 67005 (2018).

41. Chandrasekaran, A. et al. Asymmetric structure of 90 domain walls and interactions with defects in $PbTiO_3$. *Phys. Rev. B* **93**, 144102 (2016).

42. Schilling, A., Bowman, R. M., Catalan, G., Scott, J. F. & Gregg, J. M. Morphological control of polar orientation in single-crystal ferroelectric nanowires. *Nano Lett.* **7**, 3787–3791 (2007).

43. Scott, J. F. et al. Superdomain dynamics in ferroelectric-ferroelastic films: switching, jamming, and relaxation. *Appl. Phys. Rev.* **4**, 041104 (2017).

44. Schilling, A. et al. Scaling of domain periodicity with thickness measured in $BaTiO_3$ single crystal lamellae and comparison with other ferroics. *Phys. Rev. B* **74**, 024115 (2006).

45. McGilly, L. J. & Gregg, J. M. Polarization closure in $PbZr_{(0.42)}Ti_{(0.58)}O_3$ nanodots. *Nano Lett.* **11**, 4490–4495 (2011).

46. Liu, W. et al. Twin domains in organometallic halide perovskite thin-films. *Crystals* **8**, 216 (2018).

47. Ma, J. et al. Modulation of charged a1/a2 domains and piezoresponses of tensile strained $PbTiO_3$ films by the cooling rate. *RSC Adv.* **9**, 1981–13990 (2019).

48. O'Connell, E., Hennessy, M. & Eoin Moynihan. *PinkShnack/TEMUL: DOI Release.* https://doi.org/10.5281/ZENODO.3832143 (2020).

49. Grillo, V. & Rossi, F. STEM_CELL: a software tool for electron microscopy. Part 2 analysis of crystalline materials. *Ultramicroscopy* **125**, 112–129 (2013).

Author contributions

T.H. and A.J.B. grew the PTO crystal. M.C. performed the FIB sample preparation. K.M. and M.C. conducted the STEM experiments with input from C.C., J.M., A.H. and J.M.G. E.O.C. wrote the code for the image analysis. K.M. performed the data analysis and prepared the figures with E.O.C. The manuscript was written with input from all authors. U.B. supervised the project.

Competing interests

The authors declare no competing interests.

Additional information

Supplementary information is available for this paper at https://doi.org/10.1038/s42005-020-00488-x.

Correspondence and requests for materials should be addressed to K.M. or U.B.

Reprints and permission information is available at http://www.nature.com/reprints

Publisher's note Springer Nature remains neutral with regard to jurisdictional claims in published maps and institutional affiliations.